

Article

# Influence of Al Content on the Inclusion-Microstructure Relationship in the Heat-Affected Zone of a Steel Plate with Mg Deoxidation after High-Heat-Input Welding

Longyun Xu <sup>1</sup> , Jian Yang <sup>1,\*</sup> and Ruizhi Wang <sup>2</sup>

<sup>1</sup> State Key Laboratory of Advanced Special Steel, School of Materials Science and Engineering, Shanghai University, Shanghai 200444, China; xulongyun@shu.edu.cn

<sup>2</sup> Steelmaking Research Department, Research Institute, Baosteel Group Corporation, Shanghai 201900, China; wangruizhi@baosteel.com

\* Correspondence: yang\_jian@t.shu.edu.cn; Tel.: +86-021-6613-6580

Received: 21 November 2018; Accepted: 3 December 2018; Published: 6 December 2018



**Abstract:** The effects of Al content on inclusions, microstructures, and heat-affected zone (HAZ) toughness in a steel plate with Mg deoxidation have been investigated by using simulated high-heat-input welding and an automated feature system. The studies indicated that the main kind of oxysulfide complex inclusions in two steels without and with Al addition were both MgO-MnS. The number densities and mean sizes of inclusions were  $96.65 \text{ mm}^{-2}$  and  $3.47 \text{ }\mu\text{m}$ ,  $95.03 \text{ mm}^{-2}$  and  $2.03 \text{ }\mu\text{m}$ , respectively. The morphologies of MgO-MnS complex inclusions in steel were changed obviously with the addition of Al. When containing 0.001 wt.% Al, they consisted of a central single MgO particle and outside, the MnS phase. When containing 0.020 wt.% Al, they comprised several small MgO particles entrapped by the MnS phase. Because the former could nucleate intragranular acicular ferrites (IAFs) and the latter was non-nucleant, the main intragranular microstructures in HAZs were ductile IAFs and brittle ferrite side plates (FSPs), respectively. Therefore, HAZ toughness of the steel plate without Al addition after high-heat-input welding of 400 kJ/cm was significantly better than that of the steel plate with Al addition.

**Keywords:** Mg deoxidation; inclusions; Al addition; high-heat-input welding; heat-affected zone; toughness

## 1. Introduction

In steelmaking, extensive efforts have been made to remove massive inclusions, which deteriorate the final qualities of products. In this regard, Takamura et al. [1] introduced the concept termed “oxide metallurgy” for the first time at the sixth international iron and steel congress in 1990. Since then, increasing attention has been drawn to the functions of fine inclusions dispersed in steels. Nowadays, oxide metallurgy technology has been deemed as the most effective method to improve the heat-affected zone (HAZ) toughness of steel plates after high-heat-input welding [2–4]. Inclusions can act as intragranular nucleation sites for acicular ferrite, resulting in interlocked fine intragranular acicular ferrites (IAFs) and consequently improved HAZ toughness of the steel plate [5]. The characteristics including chemistry, size, and morphology of inclusions play important roles in the nucleation of IAF.

Currently, strong deoxidizers, such as Mg, have been utilized to develop advanced oxide metallurgy technology. Mg deoxidation is an effective method to control inclusions. Kim et al. [6] reported that Mg addition in Mn-Si-Ti deoxidized steels benefited the refining and modification of inclusions. With the increase of Mg content in steels, the mean size of inclusions decreased, and the number density

increased. The oxide phase of inclusions changed from  $Ti_2O_3$  to Ti-Mg-O, to  $MgTiO_3$ , and then to MgO. Chai et al. [7] also found that the addition of Mg in steel was able to refine and modify Ti-based inclusions. Besides, Park et al. [8] comprehensively investigated the evolution of inclusions in Mn-Si-Ti-Al-Mg deoxidized steel containing Mg of about 10 ppm (in mass fraction) and Al in the range of 6 and 147 ppm. They found that the major oxide inclusions changed from the Mg-Ti-O to  $MgAl_2O_4$  with increasing content of Al in steels. They also observed large MgO- $Al_2O_3$  aggregates entrapped in MnS in steels containing 87 and 147 ppm Al. Li et al. [9] studied the effect of Mg addition on the nucleation of IAF in as-cast Al-killed low carbon steel. They suggested that the Mn-depleted zone (MDZ) around the MgO- $Al_2O_3$ -MnS inclusion induced by MnS precipitation on the inclusion promoted the IAF formation. However, the influence of Al content on the relationship between inclusions and HAZ microstructures has not been comprehensively investigated in steel plates for high-heat-input welding.

In our previous study, it has been reported that HAZ toughness of Al-killed steel was deteriorated after high-heat-input welding, resulting from coarse prior-austenite grains (PAG) and brittle microstructures [10]. It was observed that the major kind of inclusions in Al-killed steel was the  $Al_2O_3$ -MnS inclusion, which was unable to nucleate an acicular ferrite during the high-heat-input welding process [10,11]. According to reports in recent literature, in Mg deoxidized steels containing a low level of Al content, Mg-containing inclusions, such as MgO-MnS [12], (Mg-Ti-O)-MnS [7], (Mg-Al-Ti-O)-MnS [11], and (Ti-Ca-Mg-O)-MnS [13], were favorable to promote the formation of IAF, resulting in enhanced HAZ toughness. However, the effect of inclusions formed in Mg deoxidized steel containing a high level of Al content on the HAZ microstructure and toughness has not yet been understood comprehensively.

In the present study, the influence of Al content on inclusions and microstructures in HAZ of steel plates with Mg deoxidation after high-heat-input welding is studied. In order to evaluate the characteristics of inclusions, two experimental steels with Mg deoxidation were prepared by the addition of Al or not. The morphology, size, composition, and number density of inclusions were investigated. Inclusions were correlated with the HAZ microstructure of each specimen in order to reveal the relationship between them. The main purpose of this paper is to clarify the role of Al content on HAZ toughness in steel plates with Mg deoxidation after high-heat-input welding of 400 kJ/cm.

## 2. Materials and Methods

### 2.1. Experimental Steel Preparation

Two kinds of experimental steels with Mg deoxidation, namely 3Mg1Al and 3Mg20Al, were melted in a 50-kg vacuum induction furnace with sintered magnesia lining, respectively. Table 1 shows the major chemical compositions of experimental steel samples. As shown in Table 1, Al contents in 3Mg1Al and 3Mg20Al were 10 and 200 ppm, respectively, and other elements were nearly kept at the same levels. Deoxidation experiments were carried out in this furnace under Ar atmosphere. Firstly, about 40 kg of pure iron were melted, and lime (CaO) was added as the top slag to assure considerably low oxygen potential in the slag. Then, the proper amount of deoxidants, Mn, Si, Al, Ti, and Mg, were added into molten steel to obtain the target composition. These melts were then cast into ingots with the size of  $120 \times 180 \times 240 \text{ mm}^3$ . Each ingot was hot rolled into a steel plate with a thickness of 50 mm. Roughing rolling was conducted at a temperature above  $930 \text{ }^\circ\text{C}$  with a reduction ratio greater than 30%, and finishing rolling was carried out at a temperature of about  $800 \text{ }^\circ\text{C}$  with a reduction ratio greater than 30%. Then, the steel plate was cooled down from  $760\text{--}400 \text{ }^\circ\text{C}$  at a cooling rate of about  $10 \text{ }^\circ\text{C/s}$ .

**Table 1.** Measured chemical compositions of steel samples (wt.%).

Steels	C	Si	Mn	P	S	Ti	Mg	Al	Als *	O	N
3Mg1Al	0.082	0.22	1.56	0.006	0.005	0.011	0.0027	0.001	0.001	0.0011	0.0032
3Mg20Al	0.082	0.22	1.56	0.006	0.004	0.011	0.0027	0.020	0.019	0.0007	0.0032

\* Als means the content of acidic soluble Al in steel.

## 2.2. Simulated High-Heat-Input Welding Experiments

In order to evaluate the HAZ toughness of experimental steel plates, simulated high-heat-input welding experiments were carried out by using of Gleeble 3800 thermal simulator (Dynamic Systems Inc., New York, NY, USA). It was designed to simulate electrogas arc welding with a heat input of 400 kJ/cm for a steel plate with a thickness of 50 mm. The steel specimen for simulated welding experiments with a size of  $11 \times 11 \times 71 \text{ mm}^3$  (Figure 1a) was cut down from a position about 1/4 width and 1/4 length from the edge of the steel plate. As shown in Figure 1a, two thermocouples were welded in the center position of the steel specimen for the simulated high-heat-input welding experiment. During the experiment, the peak welding temperature was 1400 °C with a holding time of 3 s. The cooling rates from 1400–800 °C, from 800–500 °C, and from 500–300 °C were controlled to be 3.41, 0.78, and 0.17 °C/s, respectively. Figure 1b shows the steel specimen after the simulated welding thermal cycle process. A relatively large area near the welding spot was obtained, namely HAZ. It was then machined into a standard Charpy specimen with the size of  $10 \times 10 \times 55 \text{ mm}^3$  (Figure 1c). A V-notch was opened at the location of welding spots. Then, Charpy impact tests of HAZ specimens were conducted at −20 °C. Afterward, the fracture surfaces were examined by a scanning electron microscope (SEM, EVO 18, Carl Zeiss, Oberkochen, Germany).

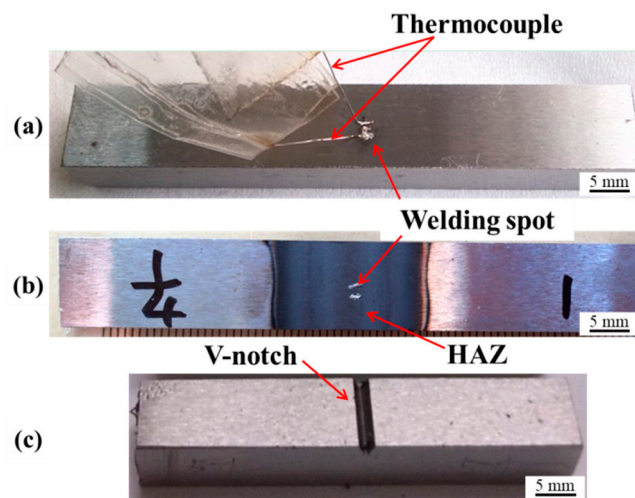


**Figure 1.** Steel specimens for the simulated high-heat-input welding experiment: (a) before welding, (b) after welding, and (c) the Charpy V-notch impact test. HAZ, heat-affected zone.

## 2.3. Characterization of Inclusions and Microstructures

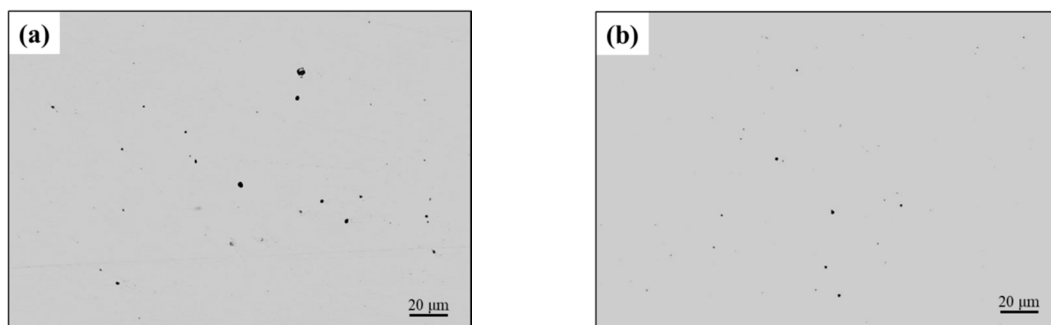
These HAZ specimens were taken from the surfaces in parallel with the fracture cross-sections after Charpy impact tests. Firstly, these specimens were polished and then analyzed by an automated feature system operating on SEM. This technique combines the advantages of energy dispersive X-ray spectrometry (EDS, Oxford Instruments, Abingdon, UK) with digital image analysis of backscattered electron (BSE) micrographs. It provides fast measurements of composition, size, and morphology simultaneously for thousands of inclusions embedded in a steel matrix [14]. Then, these specimens were slightly etched by 4-pct nital solution to observe HAZ microstructures with optical microscopy (OM, DM 2700 M, Leica, Germany) and SEM-EDS. The present study mainly focused on these

inclusions with the equal-circle diameter (ECD) larger than 1  $\mu\text{m}$ . The ECD was defined as the diameter of a circle whose area is equal to the area occupied by the inclusion in the BSE micrograph. Mapping scanning of typical inclusions in each sample was performed to examine the elemental distribution inside inclusions.

### 3. Experimental Results

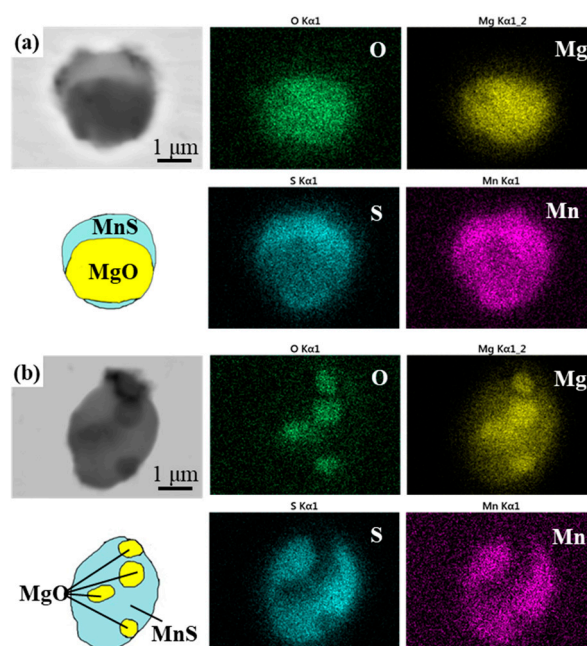
#### 3.1. Morphology and Composition of Typical Inclusions

Figure 2 shows the typical distributions of inclusions in 3Mg1Al and 3Mg20Al. Inclusions embedded in the steel matrix are observed as small black dots in the BSE micrographs. It is seen that inclusions in both steel samples are evenly distributed in steel matrixes. It is also seen that the amount of inclusions with relatively large sizes in 3Mg1Al (Figure 2a) is more than that in 3Mg20Al (Figure 2b).



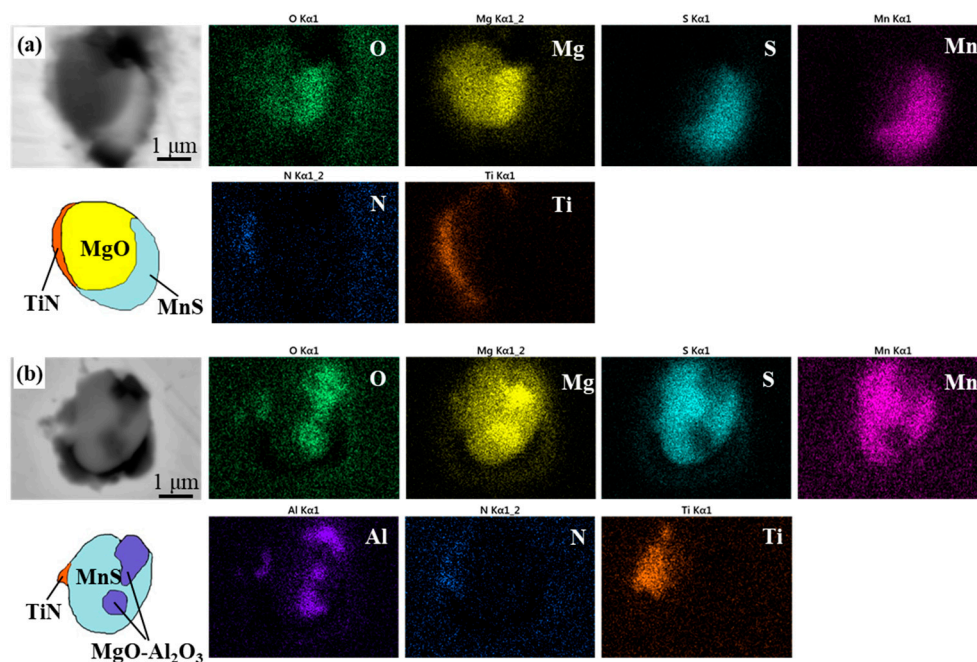
**Figure 2.** Distributions of inclusions in typical field of views with 500 magnifications in experimental steels. (a) 3Mg1Al; (b) 3Mg20Al.

Figure 3 shows the morphologies and compositions of typical MgO-MnS inclusions in 3Mg1Al and 3Mg20Al. The mapping analysis result reveals that the MgO-MnS inclusion in 3Mg1Al was composed of a central single MgO particle with a diameter about 2  $\mu\text{m}$  and a peripheral MnS phase. On the contrary, the morphology of the MgO-MnS inclusion in 3Mg20Al was quite different. It was composed of four small MgO particles with a diameter smaller than 0.5  $\mu\text{m}$  and an irregular MnS phase as the “matrix”.



**Figure 3.** Morphologies and compositions of typical MgO-MnS inclusions. (a) 3Mg1Al; (b) 3Mg20Al.

Figure 4 shows the morphologies and compositions of typical complex inclusions comprising oxide, sulfide, and nitride in 3Mg1Al and 3Mg20Al. According to the mapping analysis results, it was confirmed that the nitride phase was TiN, which was located at the edge of the complex inclusion. As shown in Figure 4a, a single MgO particle of the complex inclusion in 3Mg1Al was covered by a small amount TiN and MnS. It is seen in Figure 4b that in the complex inclusion of 3Mg20Al, two small MgO-Al<sub>2</sub>O<sub>3</sub> particles were embedded in the MnS phase, and TiN was precipitated at the edge of the MnS phase. According to the thermodynamic calculation results reported by Park et al. [8], the precipitate temperature of TiN was under the solidus of steel in Ti-Al-Mg deoxidized steels, in which the contents of Ti and N were similar to the experimental steel samples in the present study. Thus, it is reasonable that a pure TiN precipitate was hardly observed in both steels. In the present study, TiN phases were generally observed on the surfaces of MgO (Figure 4a) or MnS (Figure 4b), probably due to the lower interfacial energy [8,15].



**Figure 4.** Morphology and composition of typical inclusions. (a) MgO-MnS-TiN in 3Mg1Al; (b) MgO-Al<sub>2</sub>O<sub>3</sub>-MnS-TiN in 3Mg20Al.

### 3.2. Number Density and Size Distribution of Inclusions

Table 2 shows the statistical results of inclusions for steel samples 3Mg1Al and 3Mg20Al. They were based on the examination of inclusions with the number of 3750 and 3003 in the area of 38.8 and 31.6 mm<sup>2</sup>, respectively. The number densities of inclusions in 3Mg1Al and 3Mg20Al were 96.65 and 95.03 mm<sup>-2</sup>, respectively. The mean sizes of inclusions in both steel samples were 3.47 and 2.03 μm, respectively. Figure 5 shows the size distribution of inclusions in both experimental steels. The cumulative frequencies of inclusions with the size less than 5 μm in 3Mg1Al and 3Mg20Al were 86.61% and 96.97%, respectively. The frequencies of inclusions with the sizes between 2 and 5 μm in 3Mg1Al and 3Mg20Al were 72.29% and 29.77%, respectively. In comparison, the frequency of inclusions with the sizes between 1 and 2 μm in 3Mg20Al were as high as 63.73%. It was concluded that the inclusion size of 3Mg20Al was much smaller than that of 3Mg1Al.

Table 2. Statistical results of inclusions in experimental steels.

Steels	Area (mm <sup>2</sup> )	Number of Inclusions	Number Density (mm <sup>-2</sup> )	Mean Size (μm)
3Mg1Al	38.8	3750	96.65	3.47
3Mg20Al	31.6	3003	95.03	2.03

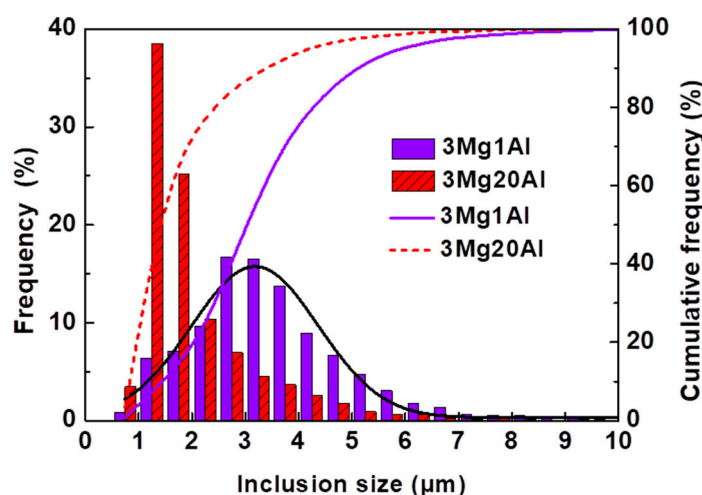


Figure 5. Size distribution of inclusions in experimental steels.

### 3.3. Composition of Inclusions

Figure 6 shows the average compositions of inclusions in 3Mg1Al and 3Mg20Al according to the statistical results of 3750 and 3003 inclusions, respectively. As shown in Figure 6a, the sums of Mg, O, Mn, and S contents of inclusions in 3Mg1Al and 3Mg20Al were 90.77 and 86.46 wt.%, respectively. It was inferred that inclusions in both steel samples were mainly composed of MgO and MnS. The average Al content of inclusions in 3Mg1Al was as low as 0.11 wt.%. Comparatively, that in 3Mg20Al was 3.51 wt.%, which was 30-times more than that in 3Mg1Al. Other major elements' contents were nearly at the same level. According to the analysis results in Section 3.1, the elemental contents of inclusions in both steels can be converted into the components of inclusions, as shown in Figure 6b. Main components of inclusions in 3Mg1Al and 3Mg20Al were both MgO and MnS. In addition, the content of Al<sub>2</sub>O<sub>3</sub> in inclusions of 3Mg1Al was much less than that of 3Mg20Al.

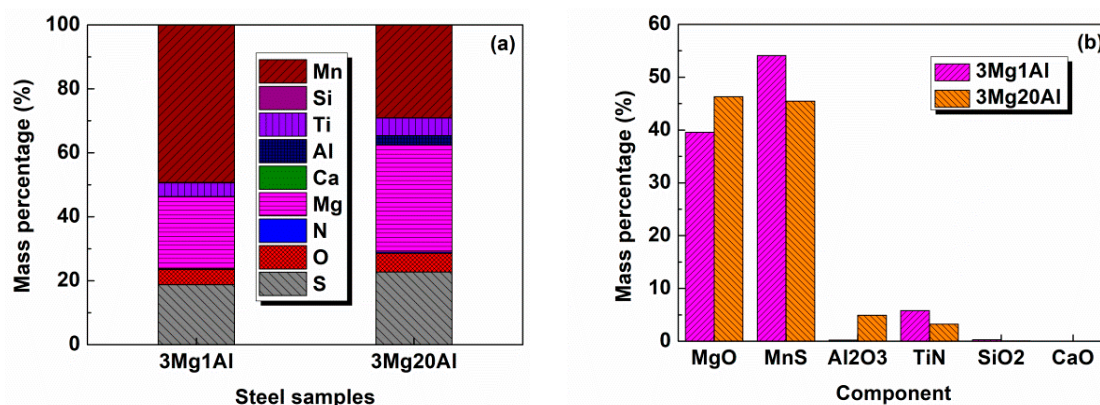
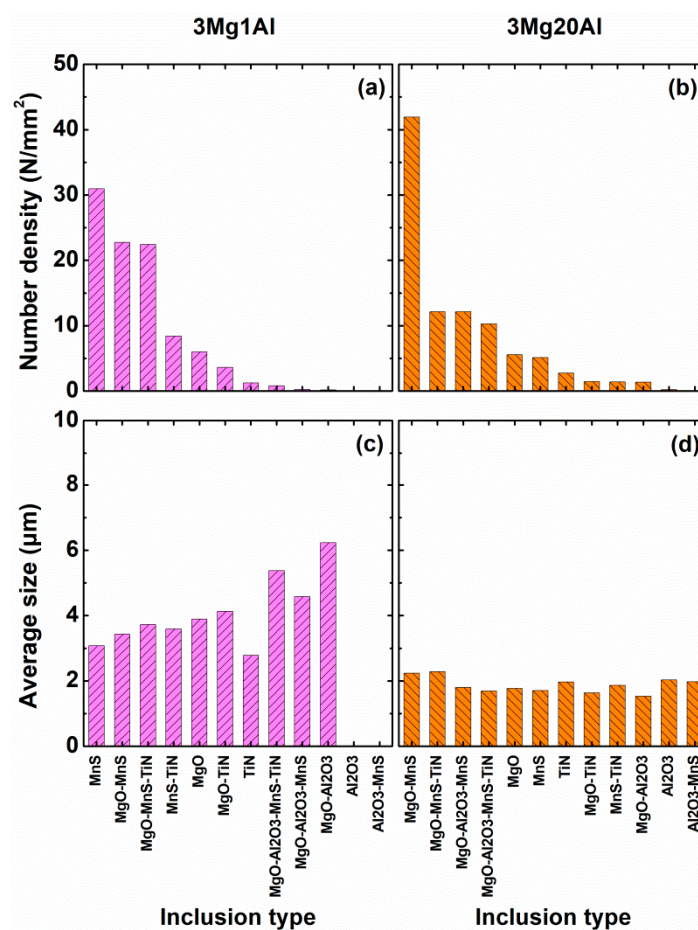


Figure 6. Comparison of the average composition of inclusions in 3Mg1Al and 3Mg20Al.

### 3.4. Types of Inclusions

According to the analysis results of inclusions' morphology and composition, these inclusions could be classified into 12 types by the major compositional elements (Mg, Al, Ti, Mn, O, N, and S),

namely (1) MgO, (2) Al<sub>2</sub>O<sub>3</sub>, (3) MgO-Al<sub>2</sub>O<sub>3</sub>, (4) MgO-MnS, (5) Al<sub>2</sub>O<sub>3</sub>-MnS, (6) MgO-Al<sub>2</sub>O<sub>3</sub>-MnS, (7) MgO-TiN, (8) MgO-MnS-TiN, (9) MgO-Al<sub>2</sub>O<sub>3</sub>-MnS-TiN, (10) MnS-TiN, (11) TiN, and (12) MnS. Figure 7 shows the number density and average size of different types of inclusions in 3Mg1Al and 3Mg20Al. The main inclusion types in 3Mg1Al were MnS, MgO-MnS, and MgO-MnS-TiN. Their number densities were 30.95, 22.73, and 22.45 mm<sup>-2</sup> with average sizes of 3.08, 3.43, and 3.73 μm, respectively, as shown in Figure 7a,c. In 3Mg20Al, the main inclusion types were MgO-MnS, MgO-MnS-TiN, and MgO-Al<sub>2</sub>O<sub>3</sub>-MnS with number densities and average sizes of 41.93, 12.15, 12.12 mm<sup>-2</sup> and 2.24, 2.29, 1.80 μm, respectively, as shown in Figure 7b,d. In comparison, inclusion types containing Al<sub>2</sub>O<sub>3</sub> were hardly found in 3Mg1Al, while they were relatively easy to observe in 3Mg20Al. In addition, the number density of MnS in 3Mg1Al, 30.95 mm<sup>-2</sup> was five-times larger than that in 3Mg20Al, 5.13 mm<sup>-2</sup>. This may be because the S content in 3Mg1Al was higher than that in 3Mg20Al, as shown in Table 1.



**Figure 7.** Number density and average size of different types of inclusions in experimental steels.

### 3.5. HAZ Microstructure and Toughness

Figure 8 shows the HAZ microstructures of experimental steels after high-heat-input welding of 400 kJ/cm. It is obvious that the grain boundary ferrites (GBFs) were network-like distributed in HAZ microstructures of 3Mg1Al and 3Mg20Al, as shown in Figure 8a,d. GBF was nucleated from the austenite grain boundary (AGB) and distributed along with AGB. Thus, prior-austenite grain (PAG) can be characterized by these network-like GBFs. It was observed that the size of PAGs in 3Mg1Al was similar to that in 3Mg20Al, though GBF in the former was finer than that in the latter. However, the microstructure inside the austenite grain in 3Mg1Al was quite different from that in 3Mg20Al. In 3Mg1Al, well-developed IAFs almost occupied the whole inner part of this austenite grain, as shown

in Figure 8b. In contrast, intragranular microstructures in 3Mg20Al were mainly composed of ferrite side plates (FSPs), which went through the grain, as shown in Figure 8e. It is seen in Figure 8c that IAFs observed at 1000 magnifications with OM showed an interlocked morphology. It is also observed that a micrometer-sized inclusion was surrounded by several acicular ferrite lathes. In Figure 8f, it is clear that lathes of FSPs showed a parallel morphology.

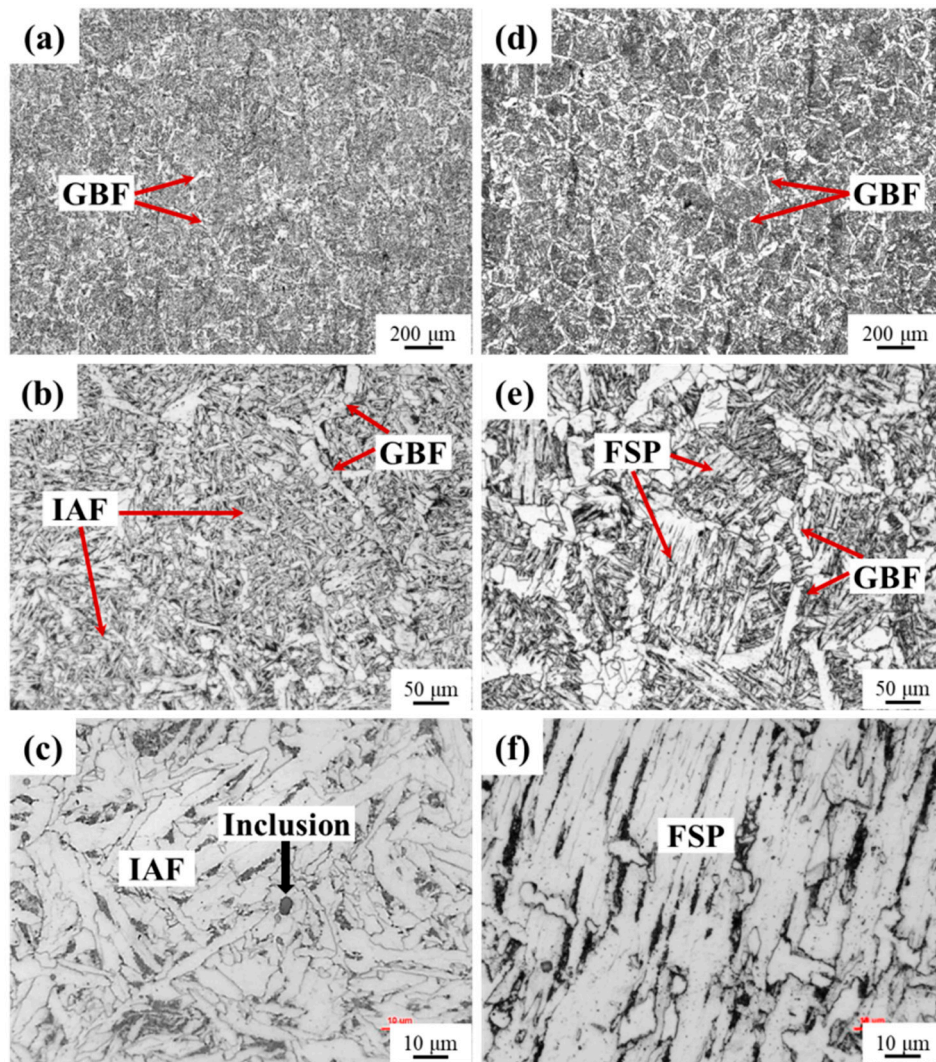


**Figure 8.** HAZ microstructures of experimental steels after high-heat-input welding with 400 kJ/cm. (a–c) 3Mg1Al; (d–f) 3Mg20Al. GBF, grain boundary ferrite; IAF, intragranular acicular ferrite; FSP, ferrite side plate.

Figure 9 shows morphologies and SEM mapping images of inclusions in HAZ microstructures for 3Mg1Al and 3Mg20Al. It was observed in a field of view of 500-times magnification in 3Mg1Al that the inclusion with a size of about 3.31  $\mu\text{m}$  was located in the inner part of austenite grain, which was occupied by IAFs, marked with a square in Figure 9a. At a magnification of 5000-times, shown in Figure 9b, this inclusion in Figure 9a was located in the center of four ferrite emanations. It was inferred that these four acicular ferrite lathes were nucleated directly from the same inclusion. This kind of inclusion was reasonably considered as an effective nucleant of IAF [16]. According to SEM mapping images of this nucleant, shown in Figure 9c, it was composed of a spherical MgO particle with a diameter of 2.38  $\mu\text{m}$  and a peripheral MnS phase.

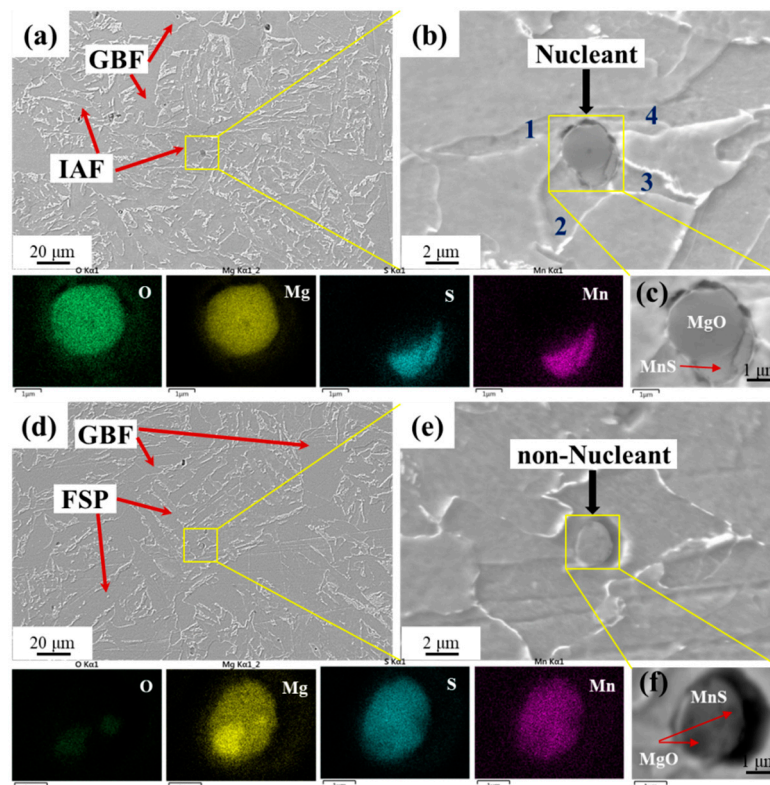


**Figure 9.** Morphologies and SEM mapping images of inclusions in HAZ microstructures for experimental steels. (a–c) 3Mg1Al; (d–f) 3Mg20Al.

The HAZ microstructure observed by SEM in 3Mg20Al is shown in Figure 9d. It is seen that parallel FSPs were surrounded by coarse GBFs. IAFs were hardly found in the HAZ microstructure of 3Mg20Al. An intragranular inclusion with a size of about 2.46  $\mu\text{m}$  was also observed. At a magnification of 5000-times, shown in Figure 9e, this inclusion was located within the ferrite matrix and without ferrite emanations. This kind of inclusion is regarded as the non-nucleant of IAF because of the absence of ferrite emanation [16]. The element mapping analysis result, shown in Figure 9f, indicates that this inclusion consisted of two small MgO particles with diameters under 1  $\mu\text{m}$  distributed in the MnS phase as the “matrix”.

Figure 10 shows the macro fractographs and SEM images of the fracture surfaces of HAZs for 3Mg1Al and 3Mg20Al. The fractograph of the specimen of 3Mg1Al after the standard Charpy impact test shows obvious transverse deformation, as indicated by apparently lateral expansion, as shown in Figure 10a. In comparison, the steel sample of 3Mg20Al had less transverse deformation, as shown in Figure 10d. The values of the lateral expansion of 3Mg1Al and 3Mg20Al were 2.26 and 0.98 mm, respectively. Table 3 shows the results of quantitative statistical analysis of fracture surfaces in 3Mg1Al and 3Mg20Al. The area fractions of the fibrous zone and the shear lip zone associated with ductile fracture in 3Mg1Al were 56.03% and 21.95%, respectively. They were 20.63% and 2.51% in 3Mg20Al. The area fraction of radical zone relating to brittle fracture in 3Mg1Al was 22.01%. That in 3Mg20Al was as high as 78.86%. The sizes of fractures in the radical zone in 3Mg1Al were smaller than those in 3Mg20Al, as shown in Figure 10b,e, respectively. Dimples were apparently observed in fibrous zones of both steel samples, as shown in Figure 10c,f, respectively. The average Charpy absorbed energy values at  $-20\text{ }^{\circ}\text{C}$  of 3Mg1Al and 3Mg20Al were 201 and 75 J, respectively. It was indicated that the HAZ toughness of 3Mg1Al was much better than that of 3Mg20Al.

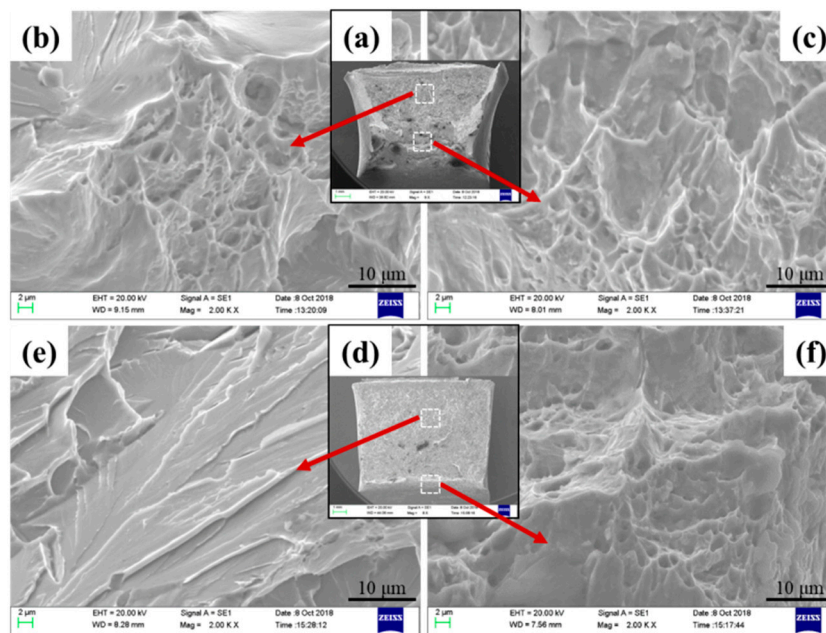


**Figure 10.** Fracture morphology features of HAZs. (a–c) 3Mg10Al; (d–f) 3Mg20Al.

**Table 3.** Results of the quantitative statistical analysis of fracture surfaces and Charpy absorbed energy of HAZ at  $-20\text{ }^{\circ}\text{C}$ .

Steels	Impact Fracture			Impact Toughness (J)	
	Fibrous Zone (%)	Shear Lip Zone (%)	Radical Zone (%)	Individual Value	Mean
3Mg1Al	56.03	21.95	22.01	195, 186, 222	201
3Mg20Al	20.63	2.51	76.86	59, 91, 75	75

## 4. Discussion

### 4.1. Effect of Al on Inclusions

Al has a relative strong affinity with oxygen in molten steel. It is a kind of strong deoxidizer widely used during the deoxidation process in steel plants.  $\text{Al}_2\text{O}_3$  is the unique direct product of Al deoxidation. Thus,  $\text{Al}_2\text{O}_3$  inclusion is the major oxide inclusion appearing in normal Al-killed steel. The strong attractive force between  $\text{Al}_2\text{O}_3$  inclusions causes the coagulation and formation of  $\text{Al}_2\text{O}_3$  clusters. However, the attractive force between a pair of  $\text{MgO-Al}_2\text{O}_3$  inclusions in Mg-added Al-killed steel and that of MgO inclusions in Mg-killed steel is only one-tenth of that between a pair of  $\text{Al}_2\text{O}_3$  inclusions, resulting in a much weaker tendency to form  $\text{MgO-Al}_2\text{O}_3$  or MgO clusters [17]. This is an effective method to refine and disperse inclusions by the use of Mg addition in steel. Thus, inclusions observed in both experimental steels 3Mg1Al and 3Mg20Al were dispersed uniformly, as shown in Figure 2. In the present study, the 3Mg1Al steel was a Mg-killed steel. It was prepared without intentional Al addition. As shown in Figure 3a, the oxide phase of inclusion is a pure MgO particle with a diameter of about  $2\text{ }\mu\text{m}$ . In our previous study, it was observed that oxide inclusions in steel containing the same level of Mg content were Mg-Ti-O or Mg-Al-Ti-O [18] when the oxygen level was up to 40 ppm. In comparison, the oxygen content in steel sample 3Mg1Al, 11 ppm, was much lower, as shown in Table 1. In addition, the affinity with oxygen of Mg was much stronger than that of Ti [19]. Therefore, MgO was preferentially formed in 3Mg1Al, when it contained relatively low oxygen content.

$\text{Al}_2\text{O}_3$  inclusions easily formed clusters and separated from molten steel by flotation [20]. Generally, the total oxygen content in steel was decreased with increasing acidic soluble Al content [21]. In addition, the coarsening rate of particles in molten steel was largely dependent on the dissolved oxygen content [22].

In the present study, Mg was added into molten steel as a final deoxidizer. Due to the relatively low level of oxygen in molten steel, the diameter of MgO particles formed in 3Mg20Al was much smaller than that in 3Mg1Al, as shown in Figure 3. Consequently, size distributions of inclusions in 3Mg1Al and 3Mg20Al were concentrated in the range from 2.5–4.5  $\mu\text{m}$  and from 1.5–2.5  $\mu\text{m}$ , respectively, as shown in Figure 5.

Oxysulfide complex inclusions are intentionally formed in oxide metallurgy technology [5,23]. As can be seen in Figure 7, the major oxysulfide complex inclusions in 3Mg1Al and 3Mg20Al were both MgO-MnS. However, the morphologies between them were quite different, as shown in Figure 3. Firstly, the oxide phase in the MgO-MnS complex inclusion in 3Mg1Al was a single MgO particle with a diameter larger than 1  $\mu\text{m}$ , as shown in Figure 3a. In 3Mg20Al, the oxide phases were several separate MgO particles with a diameter smaller than 0.5  $\mu\text{m}$ , as shown in Figure 3b. Secondly, the MnS phase in 3Mg1Al was precipitated on the surface of the MgO particle. In 3Mg20Al, several small MgO particles were entrapped by MnS. Park et al. [8] also found oxysulfide complex inclusions with a similar morphology. They observed small MgO-Al<sub>2</sub>O<sub>3</sub> granules entrapping a large MnS in the steel containing Al of more than 40 ppm. It is not certain how this kind of inclusion is formed in the present state. However, the following mechanism may be postulated. Since the dissolved oxygen content in molten steel is relatively low resulting from a relatively high level of acidic soluble Al content, a large quantity of MgO particles with small sizes was formed after final deoxidation by Mg addition. These small MgO particles were easily encapsulated by MnS during solidification. Besides, there was a very weak interaction between MgO particles, so that no MgO aggregates formed in the steel [17]. Therefore, most of the inclusions in 3Mg20Al were fine and evenly dispersed.

#### 4.2. Effect of Al on HAZ Microstructures

As shown in Figure 8, the intragranular microstructure in HAZ of 3Mg1Al was quite different from that of 3Mg20Al. In the previous studies, several mechanisms of inclusion nucleating IAF have been proposed, including (1) reduction in interfacial energy [24], (2) decrease in lattice mismatch [25], (3) lessening thermal strains [5], and (4) the formation of a solute depletion zone [26,27]. Although the exact mechanism has not been elucidated yet, it is widely accepted that the chemistry and size of inclusions play an important role in the nucleation of acicular ferrite.

According to the inert interface mechanism, an inclusion larger than 1.0  $\mu\text{m}$  is advantageous to nucleate IAF [16]. Zhang et al. [24] suggested that the optimal size for inclusion to become the nucleation site of IAF was about 3  $\mu\text{m}$ . However, TiO<sub>x</sub>-MnS with sizes from 1.0–3.0  $\mu\text{m}$  [28] and ZrO<sub>2</sub>-MnS with a size of 0.8  $\mu\text{m}$  [29] were also able to nucleate IAF. In the present study, as shown in Figure 9a–c, MgO-MnS complex inclusion with a size of 3.31  $\mu\text{m}$  can act as the nucleation center of IAFs. However, the MgO-MnS complex inclusion with a size of 2.46  $\mu\text{m}$  in 3Mg20Al was just located in the ferrite matrix and unable to nucleate acicular ferrite, as shown in Figure 9d–f. Although the difference of the size between inclusions in 3Mg1Al and 3Mg20Al was relatively small, the former was nucleant and the latter non-nucleant. Thus, it should be concluded that inclusion size was not the definitive factor for inclusions acting as nucleants in the present study.

Instead, the chemistry and morphology of inclusions may play key roles in inclusion nucleating IAF. Generally, oxysulfide complex inclusions comprising central oxides and, outside, the MnS phase are considered as effective nucleants for IAF [5,23]. As shown in Figure 9c, in 3Mg1Al, the MgO-MnS complex inclusion acting as the nucleant comprises a central MgO particle and outside, the MnS phase. However, the morphology of MgO-MnS complex inclusion in 3Mg20Al was several small MgO particles entrapped by MnS, as shown in Figure 9f. This kind of complex inclusion in 3Mg20Al was non-nucleant, as shown in Figure 9e. It was confirmed that pure MnS phase inclusion in steel matrix was unable to nucleate IAF [23]. It was inferred that the MgO-MnS complex inclusion with such a morphology shown in Figures 3 and 9 was similar to the pure MnS phase inclusion. It should be noted that in addition to chemistry and size, the morphology of inclusions also played an important role in the nucleation of acicular ferrite. In 3Mg1Al, due to well-developed IAFs induced by MgO-MnS complex inclusions in the HAZ microstructure, excellent HAZ toughness was obtained after high-heat-input

welding of 400 kJ/cm. However, in 3Mg20Al, the formation of FSP cannot be inhibited, resulting in the lack of a nucleant for IAF. As a result, the HAZ toughness of 3Mg20Al deteriorated.

## 5. Conclusions

The effects of Al content on the inclusion-microstructure relationship in the heat-affected zone (HAZ) of steel plates with Mg deoxidation after high-heat-input welding were investigated based on experimental studies. HAZ toughness was also measured after the simulated welding process with a heat input of 400 kJ/cm. The following conclusions were obtained:

1. The main inclusion types in 3Mg1Al without Al addition were MnS, MgO-MnS, MgO-MnS-TiN, and those in 3Mg20Al with Al addition were MgO-MnS, MgO-MnS-TiN, MgO-Al<sub>2</sub>O<sub>3</sub>-MnS. The number density of inclusions in 3Mg1Al, 96.65 mm<sup>-2</sup>, was similar to that in 3Mg20Al, 95.03 mm<sup>-2</sup>. However, the mean size of inclusions in the former, 3.47 μm, was larger than that in the latter, 2.03 μm.
2. Although the chemistries of the main kind of oxysulfide complex inclusions in 3Mg1Al and 3Mg20Al were both MgO-MnS, the morphologies were quite different. The former consisted of a central single MgO particle and outside, the MnS phase. The latter comprised several small MgO particles entrapped by the MnS phase.
3. Because the MgO-MnS complex inclusions in 3Mg1Al could nucleate intragranular acicular ferrites (IAFs) and these in 3Mg20Al were non-nucleant, the main intragranular microstructure in HAZs for 3Mg1Al was ductile IAFs, while that for 3Mg20Al was brittle ferrite side plates (FSPs). Therefore, the HAZ toughness of Mg deoxidized the steel plate without Al addition was much better than that with Al addition.

**Author Contributions:** L.X. performed the experiments, analyzed the experimental results, and wrote this manuscript. J.Y. contributed to the guidance, conceived of, and designed this research. R.W. performed the simulations.

**Funding:** This research received no external funding.

**Acknowledgments:** The financial support from Baosteel Group Corporation is greatly appreciated.

**Conflicts of Interest:** The authors declare no conflict of interest.

## References

1. Takamura, J.; Mizoguchi, S. Roles of Oxides in Steels Performance. In Proceedings of the Sixth International Iron and Steel Congress, Nagaya, Japan, 21–26 October 1990.
2. Kojima, A.; Kiyose, A.; Uemori, R.; Minagawa, M.; Hoshino, M.; Nakashima, T.; Ishida, K.; Yasui, H. Super high HAZ toughness technology with fine microstructure imparted by fine particles. *Shinmittetsu Giho* **2004**, 2–5.
3. Suzuki, S.; Ichimiya, K.; Akita, T. High tensile strength steel plates with excellent HAZ toughness for shipbuilding. *JFE Tech. Rep.* **2005**, 5, 24–29.
4. Yang, J.; Zhu, K.; Wang, R.Z.; Shen, J.G. Improving the toughness of heat affected zone of steel plate by use of fine inclusion particles. *Steel Res. Int.* **2011**, 82, 552–556. [[CrossRef](#)]
5. Sarma, D.S.; Karasev, A.V.; Jönsson, P.G. On the role of non-metallic inclusions in the nucleation of acicular ferrite in steels. *ISIJ Int.* **2009**, 49, 1063–1074. [[CrossRef](#)]
6. Kim, H.S.; Chang, C.H.; Lee, H.G. Evolution of inclusions and resultant microstructural change with Mg addition in Mn/Si/Ti deoxidized steels. *Scripta Mater.* **2005**, 53, 1253–1258. [[CrossRef](#)]
7. Chai, F.; Yang, C.F.; Su, H.; Zhang, Y.Q.; Xu, Z. Effect of magnesium on inclusion formation in Ti-killed steels and microstructural evolution in welding induced coarse-grained heat affected zone. *J. Iron Steel Res. Int* **2009**, 16, 69–74. [[CrossRef](#)]
8. Park, S.C.; Jung, I.H.; Oh, K.S.; Lee, H.G. Effect of Al on the evolution of non-metallic inclusions in the Mn-Si-Ti-Mg deoxidized steel during solidification: Experiments and thermodynamic calculations. *ISIJ Int.* **2004**, 44, 1016–1023. [[CrossRef](#)]

9. Li, X.B.; Min, Y.; Yu, Z.; Liu, C.J.; Jiang, M.F. Effect of Mg addition on nucleation of intra-granular acicular ferrite in Al-killed low carbon steel. *J. Iron Steel Res. Int.* **2016**, *23*, 415–421. [[CrossRef](#)]
10. Xu, L.Y.; Yang, J.; Wang, R.Z.; Wang, Y.N.; Wang, W.L. Effect of Mg content on the microstructure and toughness of heat-affected zone of steel plate after high heat input welding. *Metall. Mater. Trans. A* **2016**, *47*, 3354–3364. [[CrossRef](#)]
11. Xu, L.Y.; Yang, J.; Wang, R.Z.; Wang, W.L.; Wang, Y.N. Effect of Mg addition on formation of intragranular acicular ferrite in heat-affected zone of steel plate after high-heat-input welding. *J. Iron Steel Res. Int.* **2018**, *25*, 433–441. [[CrossRef](#)]
12. Xu, L.Y.; Yang, J.; Wang, R.Z.; Wang, W.L.; Ren, Z.M. Effect of welding heat input on microstructure and toughness of heated-affected zone in steel plate with Mg deoxidation. *Steel Res. Int.* **2017**, *88*, 1700157. [[CrossRef](#)]
13. Lou, H.; Wang, C.; Wang, B.; Wang, Z.; Li, Y.; Chen, Z. Inclusion Evolution behavior of Ti-Mg oxide metallurgy steel and its effect on a high heat input welding HAZ. *Metals* **2018**, *8*, 534. [[CrossRef](#)]
14. Van, E.M.; Guo, M.; Zinngrebe, E.; Blanpain, B.; Jung, I. Evolution of non-metallic inclusions in secondary steelmaking: Learning from inclusion size distributions. *ISIJ Int.* **2013**, *53*, 1974–1982.
15. Pervushin, G.V.; Suito, H. Effect of primary deoxidation products of  $Al_2O_3$ ,  $ZrO_2$ ,  $Ce_2O_3$  and MgO on TiN precipitation in Fe-10 mass% Ni alloy. *ISIJ Int.* **2001**, *41*, 748–756. [[CrossRef](#)]
16. Lee, T.K.; Kim, H.J.; Kang, B.Y.; Hwang, S.K. Effect of inclusion size on the nucleation of acicular ferrite in welds. *ISIJ Int.* **2000**, *40*, 1260–1268. [[CrossRef](#)]
17. Kimura, S.; Nakajima, K.; Mizoguchi, S. Behavior of alumina-magnesia complex inclusions and magnesia inclusions on the surface of molten low-carbon steels. *Metall. Mater. Trans. B* **2001**, *32*, 79–85. [[CrossRef](#)]
18. Yang, J.; Xu, L.Y.; Zhu, K.; Wang, R.Z.; Zhou, L.J.; Wang, W.L. Improvement of HAZ toughness of steel plate for high heat input welding by inclusion control with Mg deoxidation. *Steel Res. Int.* **2015**, *86*, 619–625. [[CrossRef](#)]
19. Karasev, A.V.; Suito, H. Characteristics of fine oxide particles produced by Ti/M (M = Mg and Zr) complex deoxidation in Fe-10 mass%Ni alloy. *ISIJ Int.* **2008**, *48*, 1507–1516. [[CrossRef](#)]
20. Ohta, H.; Suito, H. Characteristics of particle size distribution of deoxidation products with Mg, Zr, Al, Ca, Si/Mn and Mg/Al in Fe-10 mass% Ni alloy. *ISIJ Int.* **2006**, *46*, 14–21. [[CrossRef](#)]
21. Wang, Y.; Tang, H.; Wu, T.; Wu, G.; Li, J. Effect of acid-soluble aluminum on the evolution of non-metallic inclusions in spring steel. *Metall. Mater. Trans. B* **2017**, *48*, 943. [[CrossRef](#)]
22. Ohta, H.; Suito, H. Effects of dissolved oxygen and size distribution on particle coarsening of deoxidation product. *ISIJ Int.* **2006**, *46*, 42–49. [[CrossRef](#)]
23. Lee, J.L.; Pan, Y.T. Effect of sulfur content on the microstructure and toughness of simulated heat-affected zone in Ti-killed steels. *Metall. Trans. A* **1993**, *24*, 1399–1408. [[CrossRef](#)]
24. Zhang, C.; Gao, L.; Zhu, L. Effect of inclusion size and type on the nucleation of acicular ferrite in high strength ship plate steel. *ISIJ Int.* **2018**, *58*, 965–969. [[CrossRef](#)]
25. Zhu, L.; Wang, Y.; Wang, S.; Zhang, Q.; Zhang, C. Research of microalloy elements to induce intragranular acicular ferrite in shipbuilding steel. *Ironmaking Steelmaking* **2017**, 1–9. [[CrossRef](#)]
26. Kang, Y.B.; Lee, H.G. Thermodynamic analysis of Mn-depleted near Ti oxide inclusions for intragranular nucleation of ferrite in steel. *ISIJ Int.* **2010**, *50*, 501–508. [[CrossRef](#)]
27. Mabuchi, H.; Uemori, R.; Fujioka, M. The role of Mn depletion in intra-granular ferrite transformation in the heat affected zone of welded joints with large heat input in structural steels. *ISIJ Int.* **1996**, *36*, 1406–1412. [[CrossRef](#)]
28. Zheng, C.C.; Wang, X.M.; Li, S.R.; Shang, C.J.; He, X.L. Effects of inclusions on microstructure and properties of heat-affected-zone for low-carbon steels. *Sci. Chin. Technol. Sci.* **2012**, *55*, 1556–1565. [[CrossRef](#)]
29. Shi, M.H.; Zhang, P.Y.; Zhu, F.X. Toughness and microstructure of coarse grain heat affected zone with high heat input welding in Zr-bearing low carbon steel. *ISIJ Int.* **2014**, *54*, 188–192. [[CrossRef](#)]

